Revision 2

Word Count: 5500

Zhengminghuaite, $Cu_6Fe_3As_4S_{12}$, a new sulfosalt mineral from the Zimudang Carlin-type gold deposit in southwestern Guizhou, China

XUEXIANG GU[1, 2*], YONGMEI ZHANG[1, 2], GUANG FAN[3], TING LI[3], SHUYI DONG[4], YIWEI PENG[4], YINGSHUAI ZHANG [2], LING LI[2], AND ZHANLIN GE[5]

[1]State Key Laboratory of Geological Processes and Mineral Resources, China University of Geosciences, Beijing 100083, China

[2]School of Earth Sciences and Resources, China University of Geosciences, Beijing 100083, China

[3]Beijing Research Institute of Uranium Geology, Beijing 100029, China

[4]College of Earth Sciences, Chengdu University of Technology, Chengdu 610059, China

[5]Xi'an Center of Mineral Resources Survey, China Geological Survey, Xi'an 710100, China

*E-mail: xuexiang_gu@163.com

ABSTRACT

Zhengminghuaite, ideally $Cu_6Fe_3As_4S_{12}$, is a new Cu-Fe arsenosulfosalt found in the Zimudang Carlin-type gold deposit in southwestern Guizhou, China. It occurs as irregular, commonly fractured grains of several to a few tens μm in the brecciated

gold ores and is paragenetically associated with the late ore-stage mineral assemblage including realgar, orpiment, pyrite, chalcopyrite, arsenopyrite, aktashite, christite, quartz, and calcite. Zhengminghuaite is opaque with a metallic lustre and a conchoidal or uneven fracture. The Vickers microhardness (VHN_{10}) is 219 kg/mm^2 (range 192–247 kg/mm^2) and the calculated density is 4.77(5) g/cm^3. In reflected light, zhengminghuaite is whitish gray with weak bireflectance (whitish gray to pinkish tinted gray), very weak anisotropy, and no internal reflection. Electron microprobe analyses gave the empirical formula $(Cu_{5.92}Hg_{0.08})_{\Sigma 6.00}(Fe_{1.59}Hg_{1.07}Zn_{0.37})_{\Sigma 3.03}(As_{3.94}Sb_{0.02})_{\Sigma 3.96}S_{11.93}$ on the basis of total cations = 13, with the simplified formula $Cu_6(Fe,Hg,Zn)_3(As,Sb)_4S_{12}$. Zhengminghuaite is trigonal, with space group $R3$. Unit-cell parameters determined from the single-crystal X-ray diffraction data are as follows: a = 13.5373(17) Å, c = 9.2354(13) Å, and V = 1465.7(4) Å^3 (Z = 3). The eight strongest lines in the X-ray diffraction pattern are [d (Å) (I, %) (hkl)]: 3.0785 (67) (003), 3.0670 (100) $(\bar{1}31)$, 2.6586 (89) $(\bar{1}32)$, 1.8825 (97) (134), 1.8773 (82) (520), 1.6060 (89) $(13\bar{5})$, 1.6028 (81) (523), and 1.6012 (83) $(26\bar{1})$. The crystal structure of zhengminghuaite belongs to the nowackiite group and can be described as formed by (0001) layers composed of corner-sharing FeS_4 and CuS_4 tetrahedra that delimit two triangular cavities. Zhengminghuaite is the Fe-dominant analogue at the divalent cations site of nowackiite ($Cu_6Zn_3As_4S_{12}$) and aktashite ($Cu_6Hg_3As_4S_{12}$). Paragenetic relationships indicate that zhengminghuaite and associated Hg- and Tl-sulfosalts precipitated in response to the increase in sulfidation state and decrease in temperature of the late-ore

stage hydrothermal fluid.

KEY WORDS: zhengminghuaite, nowackiite group, sulfosalt, crystal-structure refinement, Carlin-type gold deposit, Zimudang, Southwest China.

INTRODUCTION

Sulfosalts are a large family of minerals that have been reported in a wide variety of hydrothermal gold and other metal deposits, including porphyry Cu-(Mo-Au) deposits (Sillitoe, 2000; Sinclair, 2007), volcanogenic massive sulfide (VMS) deposits (Hannington et al., 1997; Franklin et al., 2005; Dubé et al., 2007; Galley et al., 2007), epithermal gold and Cu-Pb-Zn-(Au-Ag) deposits (Cooke and Simmons, 2000; Taylor, 2007; Zhang et al., 2017; Slater et al., 2019; Altenberger et al., 2022), orogenic lode gold deposits (Jian et al., 2014), intrusion-related gold deposits (Thompson and Newberry, 2000; Li et al., 2019), etc. Carlin-type gold deposits often contain Hg-Tl-As-Sb sulfides (e.g., realgar, orpiment, stibnite, cinnabar, and carlinite) and sulfosalts (e.g., aktashite $Cu_6Hg_3As_4S_{12}$, christite $HgTlAsS_3$, laffittite $AgHgAsS_3$, galkhaite $(Cs,Tl)(Hg,Cu,Zn,Tl)_6(As,Sb)_4S_{12}$, lorandite $TlAsS_2$, weissbergite $TlSbS_2$, and ellisite Tl_3AsS_3; Botinelly et al., 1973; Radtke et al., 1974, 1977; Dickson and Radtke, 1978; Dickson et al., 1979; Balić-Žunić et al., 1995; Hofstra and Cline, 2000; Maroun et al., 2017; Vikentyev et al., 2019), consistent with the typically anomalous enrichment of Hg-Tl-As-Sb in this type of gold deposits. For example, The Vorontsovskoye gold deposit in Northern Urals, Russia contains 75 sulfosalt minerals including abundant Hg-Tl-As-Sb sulfosalts (Kasatkin et al., 2022a, b; and references therein).

In this contribution, we describe the new Cu-Fe-sulfosalt mineral zhengminghuaite

that was found at the Zimudang Carlin-type gold deposit in southwestern Guizhou, China. This deposit, with a reserve of over 60t Au at a grade of ~6 g/t, lies in the region called the Gold Triangle at the junction of the Yunnan, Guizhou and Guangxi Provinces in southwest China that contains numerous sedimentary rock-hosted, disseminated gold deposits similar to those in Nevada, USA. The new mineral is named in honor of Prof. Zheng Minghua (born October 23, 1934), a famous geologist and expert of gold deposits from the College of Earth Sciences, Chengdu University Technology, China. Both the name and the new mineral (the proposal IMA 2022-047) were approved by the Commission on New Minerals, Nomenclature and Classification of the International Mineralogical Association (IMA-CNMNC). The holotype specimen is deposited in the collections of the Geological Museum of China, Yangrou Hutong No. 16, Xisi, Beijing 100031, People's Republic of China, with registration number 16136.

OCCURRENCE

Specimens containing zhengminghuaite were collected from the underground tunnel of the Zimudang gold deposit, approximately 220 km southwest of the capital city Guiyang of Guizhou Province, southwestern China (105°28′53.4″E, 25°34′33.6″N). A detailed description of geology, geochemistry, and ore genesis of the deposit can be found elsewhere (e.g., Peters et al., 2007; Su et al., 2009; Gu et al., 2012; Cline et al., 2013; Peng et al., 2014; Liu et al., 2015). The deposit is hosted in Upper Permian and Lower Triassic thin- to medium-bedded, organic-rich, bioclastic limestone and marl interbedded with calcareous siltstone and shale. Gold

mineralization occurs both as stratabound ore layers and as lens-shaped ore bodies within fault and fracture zones in altered rocks (Fig. 1a). Hydrothermal mineral assemblages of the deposit include an early stage of quartz ± pyrite, a main ore-stage of auriferous quartz + arsenian pyrite + arsenopyrite + marcasite, and a late ore-stage of quartz + calcite + realgar ± orpiment ± native arsenic ± stibnite ± cinnabar ± dolomite. The early stage quartz, occasionally containing anhedral to euhedral, Au- and As-poor pyrite, occurs most commonly as milky white narrow veins/veinlets and is locally fractured and cemented or crosscut by the main-ore and late-ore stage minerals. The main-ore stage assemblage consists of gold-bearing arsenian pyrite, arsenopyrite, and marcasite that are most commonly enclosed in pervasive or patchy jasperoidal quartz and, less commonly, disseminated in quartz veinlets in the ore. The late-ore stage quartz, calcite, realgar, and minor to trace amounts of orpiment, chalcopyrite, pyrite, stibnite, aktashite, christite, native arsenic, and cinnabar commonly fill open spaces created by fracturing and limestone dissolution, either as ore breccia cements or as the veins/veinlets that locally crosscut and/or enclose the early and main ore-stage mineral assemblages (Fig. 1b-d). Paragenetic sequences of the hydrothermal minerals are summarized in Figure 2. The gold ore is considered to have precipitated in an immiscible, gold- and hydrocarbon-bearing, basinal fluid system (Gu et al., 2012, 2013; Peng et al., 2014).

Zhengminghuaite was found in fault-controlled gold ores composed of limestone and marl breccias cemented mainly by realgar and minor orpiment (Fig. 1b). It is observed only under microscope and paragenetically associated with the late ore-stage

mineral assemblage, including realgar, pyrite, chalcopyrite, arsenopyrite, aktashite, quartz, and calcite (Fig. 3).

PHYSICAL AND OPTICAL PROPERTIES

Under the microscope, zhengminghuaite occurs as irregular, commonly fractured grains ranging from several to a few tens μm in size (Fig. 3). It is opaque in transmitted light and exhibits a metallic lustre. No cleavage is observed, and the fracture is conchoidal or uneven. The new mineral is brittle and does not exhibit any fluorescence under UV radiation. The Vickers microhardness (VHN, 10 g load) is 219 kg/mm^2 (range 192–247 kg/mm^2), corresponding to a Mohs hardness of ~4. The density calculated based on the empirical formula (Z = 3) and the unit-cell volume determined from the single-crystal X-ray diffraction (XRD) data is 4.77(5) g/cm^3.

In reflected light, zhengminghuaite is whitish gray in color, with weak bireflectance (whitish gray to pinkish tinted gray). Anisotropy is very weak and only visible with slightly opened analyzer. No internal reflection is observed under crossed polars. Quantitative reflectance measurements were performed in oil (refractive index 1.518) relative to a SiC standard using a CRAIC508PV CoalPro microspectrophotometer (USA) equipped on a Nikon Eclipse Ni-U ore microscope (Japan). Reflectance percentages of R_{max} and R_{min} for the four wavelengths required by the IMA-COM are 28.84, 22.11 (470 nm); 29.00, 23.04 (546 nm); 31.71, 26.31 (589 nm); and 34.38, 28.31 (650 nm).

CHEMICAL COMPOSITION

The chemical composition of zhengminghuaite was determined using a JXA-8100 electron microprobe (EMP) at the Analytical Center of Beijing Research Institute of Uranium Geology, operating in wavelength-dispersive mode with an acceleration voltage 20 kV, a beam current 10 nA, and a beam diameter 1 μm. The standards employed were: cinnabar for S and Hg, synthetic GaAs for As, synthetic Sb_2Te_3 for Sb, chalcopyrite for Cu, marcasite for Hg, and sphalerite for Zn. Analytical data for 8 points are given in Table 1.

The empirical formula (based on the total cations = 13) is $(Cu_{5.92}Hg_{0.08})_{\Sigma 6.00}(Fe_{1.59}Hg_{1.07}Zn_{0.37})_{\Sigma 3.03}(As_{3.94}Sb_{0.02})_{\Sigma 3.96}S_{11.93}$. The simplified formula is $Cu_6(Fe,Hg,Zn)_3(As,Sb)_4S_{12}$. The ideal formula is $Cu_6Fe_3As_4S_{12}$, which requires Cu 30.92, Fe 13.58, As 24.30, S 31.20, total 100 wt.%.

X-RAY DIFFRACTION AND STRUCTURAL REFINEMENT

The powder XRD data for zhengminghuaite given in Table 2 were calculated based on single-crystal structural refinement data. A single-crystal fragment of zhengminghuaite with an approximate dimension of 0.005×0.010×0.015 mm, extracted from the same polished section for the EMP analysis using a Focus ion beam field emission scanning electron microscope at the Institute of Microstructure and Property of Advanced Materials, Beijing University of Technology, was used for the single-crystal XRD experiment. The diffraction experiment was performed at room temperature using a Bruker D8 QUEST diffractometer (IμS Tube, 100W, Mo*Kα*,

λ = 0.71073 Å) and a PHOTON 100 CMOS detector at the Analytical Center of Beijing Research Institute of Uranium Geology. The crystal structure of zhengminghuaite was determined and refined using the SHELX Software (Sheldrick, 2015a, b). Details of the data collection and crystal structure refinement are given in Appendix Table 1.

The total exposure time was 16.62 h. The frames were integrated with the Bruker SAINT Software Package using a narrow-frame algorithm. The integration of the data using a trigonal unit-cell yielded a total of 6250 reflections to a maximum θ angle of 30.48° (0.70 Å resolution), of which 1977 reflections were independent (average redundancy 3.161, completeness = 100.0%, R_{int} = 10.04%, R_{sig} = 14.05%) and 822 data (41.58%) were greater than 2σ (F^2). The final cell constants of a = 13.5373(17) Å, c = 9.2354(13) Å, and V = 1465.7(4) Å^3 (Z = 3) are based upon the refinement of the XYZ-centroids of 432 reflections above 20 $\sigma(I)$ with 8.235°<2θ<54.99°. Data were corrected for absorption effects using the Multi-Scan method (SADABS). The ratio of minimum to maximum apparent transmission was 0.441.

The structure was solved and refined by the Bruker SHELXTL Software Package, using the space group $R3$, with Z = 3 for the formula unit, $Cu_6Fe_{1.98}Hg_{1.02}As_4S_{12}$. The final anisotropic full-matrix least-squares refinement on F^2 with 78 variables converged at R_1 = 0.0690 and wR_2 = 0.0784 for the observed data. The goodness-of-fit was 0.931. The largest peak in the final difference electron density synthesis was 1.219 e$^-$/Å^3 and the largest hole was -1.106 e$^-$/Å^3 with an RMS deviation of 0.270 e$^-$/Å^3. On the basis of the final model, the calculated density

172 was 4.694 g/cm^3 and F(000) was 1893 e$^-$. Atom coordinates, site occupancies, and
173 displacement parameters are given in Appendix Table 2. Selected bond distances are
174 listed in Table 3, and refined site-scattering values are given in Table 4. The
175 Crystallographic Information File (CIF) is available as Supplemental Material.

176 The structure refinement revealed that Fe and Hg are at the same Me^{2+} site, but
177 Fe>Hg. The crystal structure of zhengminghuaite belongs to the nowackiite group
178 with the ideal formula $Cu_6Fe_3As_4S_{12}$. It can be described as formed by (0001) layers
179 composed of corner-sharing FeS_4 and CuS_4 tetrahedra, delimiting two triangular
180 cavities (Fig. 4). In the larger one, three As1 polyhedra are hosted, whereas the
181 smaller one hosts a single As2 site (Biagioni, 2014). The bond-lengths of Cu1 and
182 Cu2 tetrahedra range from 2.272(8) to 2.349(8) Å and from 2.316(11) to 2.332(9) Å,
183 respectively. The Fe tetrahedron bond-length ranging from 2.378(8) to 2.432(11) Å is
184 shorter than the Hg tetrahedron bond-length of aktashite (2.470(2) to 2.502(2) Å)
185 observed by Biagioni et al. (2014), indicating the substitution of a smaller cation Fe^{2+}
186 (0.63 Å) for Hg^{2+} (0.96 Å). The two independent As sites show bond distances
187 ranging from 2.253(7) to 2.298(9) Å and are bonded, through corner-sharing, with
188 CuS_4 and FeS_4 tetrahedra. The unusual feature of zhengminghuaite with the same
189 structure as aktashite is that $[AsS_3]^{3-}$ ions are grouped as quadruplets $[(AsS_3)_4]^{12-}$ (Fig.
190 5), where highly charged cations As^{3+} form tetrahedral $[As_4]^{12+}$ cluster with a vacant
191 anion position in the center (Gabuda et al, 2009).

DISCUSSION

Relation to other species

According to the IMA-COM Sulfosalt Sub-Committee report (Moëlo et al., 2008), sulfosalt mineral species is subdivided into large chemical groups. Within each group, subdivisions are generally based on well-defined structure types. Zhengminghuaite belongs to the nowackiite isotypic series of Cu-rich sulfosalts with an excess of small (univalent) cations (Cu) relative to (As), in which the ratio (Σ*Me*)/S is > 1.

There are three named species in the nowackiite isotypic series sulfosalts before the approval of zhengminghuaite. They are nowackiite, $Cu_6Zn_3As_4S_{12}$ (Marumo, 1967), aktashite, $Cu_6Hg_3As_4S_{12}$ (Kaplunnik et al., 1980), and gruzdevite, $Cu_6Hg_3Sb_4S_{12}$ (Spiridonov et al., 1981). In the system of Smith and Nickel (2007), a mineral similar to zhengminghuaite is not found. According to "The IMA-CNMNC dominant-constituent rule revisited and extended" (Hatert and Burke, 2008; Nickel and Grice, 1998), zhengminghuaite can be regarded as a new member of nowackiite isotypic series. It is the Fe-dominant analogue at the divalent cations site of nowackiite and aktashite (Table 5). Zhengminghuaite shows a regular tetrahedral coordination around Fe site with an average <Fe-S> bond distance of 2.397 Å that is shorter than the <Hg-S> bond distance of 2.481 Å in aktashite (Biagioni et al., 2014) but is slightly longer than the <Zn-S> bond distance of 2.34 Å in nowackiite (Marumo, 1967). This is in agreement with the decreasing order of ionic radii of Hg^{2+} (0.96 Å) > Fe^{2+} (0.63 Å) > Zn^{2+} (0.60 Å) in tetrahedral site (Shannon, 1976), suggesting that the

smaller the divalent cations, the shorter the <Me^{2+}-S> bond distances.

Ore paragenetic sequence and formation of zhengminghuaite

Integrated petrographic studies on textures, crosscutting relationships, and mineral assemblages of the Zimudang gold deposit indicate that zhengminghuaite, accompanied by quartz, realgar, calcite, and minor to trace amounts of orpiment, chalcopyrite, pyrite, arsenopyrite, stibnite, aktashite, christite, native arsenic, and cinnabar, formed in the late ore-stage after the deposition of bulk Au-bearing arsenian pyrite and arsenopyrite. The late ore-stage started with the precipitation of quartz that typically occurs as open space-filling, euhedral crystals (drusy quartz) concentrated on the walls of fractures and pores or rimmed on wall-rock breccias. In some instances, tiny (commonly <5 μm), euhedral to subhedral pyrite and arsenian pyrite grains are present along the growth zones of drusy quartz, indicating that gold mineralization may have continued to the early phase of the late ore-stage (Gu et al., 2012). The drusy quartz was commonly overgrown by realgar and calcite, with minor to trace amounts of Cu-Fe-Hg-Tl-As sulfides and sulfosalts, suggesting decreasing Au and increasing As, Hg, and Tl in the ore fluid as realgar and associated sulfides and sulfosalts formed. Overgrowth relationships show a typical paragenetic sequence from early to late of drusy quartz + pyrite ± arsenopyrite ± chalcopyrite, zhengminghuaite + aktashite + christite + native arsenic ± stibnite ± cinnabar, and realgar + orpiment + calcite, though formation of these minerals often overlapped with each other (Fig. 2).

Under the microscope in the studied specimen, zhengminghuaite is observed almost always together with chalcopyrite, realgar, and anhedral pyrite that has irregular fuzzy

crystal boundaries (Fig. 3). Chalcopyrite was typically replaced by zhengminghuaite, whereas the latter was commonly fractured and cemented or replaced by realgar, but at least partially is in mutual contact with realgar. This observation suggests that the formation of zhengminghuaite postdated chalcopyrite, but was prior to and partly overlapped with the precipitation of realgar. Such a relationship implies that the following reaction may have existed:

$$6CuFeS_2 + 6As + 4S_2 = Cu_6Fe_3As_4S_{12} + 2AsS + 3FeS_2 \quad (1)$$

The precipitation of zhengminghuaite can be caused by increase in sulfur fugacity (f_{S2}) or by continuous decrease in temperature. Fluid inclusion studies showed that the Carlin-type gold deposits in the southwestern Guizhou formed from low temperature (typically <250 ℃) fluids with low salinities (mostly <6 wt% NaCl equivalent) (Su et al., 2009; Gu et al., 2012; Peng et al., 2014). Two-phase, liquid-rich aqueous inclusions and two- or three-phase aqueous-carbonic (H_2O-CO_2) inclusions of the main ore-stage quartz veinlets at Zimudang homogenized mostly between 180 and 240 ℃ with a mode around 210 ℃ (Peng et al., 2014). Fluid inclusions in the late ore-stage drusy quartz from the nearby Shuiyindong gold deposit has a similar homogenization temperature range of 190 to 245 ℃ with a mode around 220 ℃ (Su et al., 2009), while those in the late ore-stage calcite coexisting with realgar at Zimudang homogenized mostly between 120 and 180 ℃ with a mode around 150 ℃ (Peng et al., 2014). As indicated in Figure 6, the transition from the deposition of drusy quartz + pyrite ± arsenopyrite to the bulk deposition of realgar during the late ore-stage could be caused by a combination of decrease in temperature and increase in

sulfur fugacity (f_{S2}) of the hydrothermal fluid. Decrease in temperature alone could not explain the bulk deposition of realgar, whereas increase in sulfidation state alone is inconsistent with the wide variation in temperature as recorded by fluid inclusions. Consequently, it is reasonable to infer that zhengminghuaite and associated sulfosalts (aktashite and christite) formed during the transition from Fe-Cu sulfides (pyrite ± arsenopyrite ± chalcopyrite) to As-sulfides (realgar ± orpiment) due to the decreasing temperature and increasing sulfidation state (more oxidized conditions) of the late ore-stage hydrothermal fluid.

Gold-bearing arsenian pyrite and arsenopyrite of the main ore-stage as well as pyrite ± arsenopyrite in the early phase of the late ore-stage probably formed from an ore fluid with f_{S2} between the pyrrhotite-pyrite and arsenopyrite-pyrite-arsenic buffers, which is constrained approximately between −15 and −13.8 log units at 210-220 °C (Fig. 6), suggesting that gold mineralization took place under a relatively oxidizing condition (intermediate sulfidation state). The lower limit of f_{S2} for the bulk deposition of realgar ± orpiment is constrained by the chalcopyrite-pyrite-bornite buffer, while the maximum f_{S2} is somewhere slightly above the realgar-orpiment buffer, which constrains f_{S2} to between −13.5 and −11.5 log units at 150 °C and suggests a high sulfidation state and moderately oxidizing conditions. However, the occurrence of orpiment only in trace amounts implies that conditions were rarely oxidizing enough to result in the bulk deposition of orpiment. Therefore, deposition of zhengminghuaite and associated sulfosalts (aktashite and christite) at Zimudang took place most probably during the transition as f_{S2} of the ore fluid increased by 1-2 log

280 units and the temperature decreased from 220 to 150 °C.

281 ## IMPLICATIONS

282 The discovery of zhengminghuaite and its paragenetic relationship to other ore and
283 gangue minerals provide insights into the evolution history of hydrothermal fluids and
284 the physicochemical conditions of ore formation for the Carlin-type gold deposits.
285 After the bulk gold mineralization of the main ore-stage, the appearance of drusy
286 quartz with minor pyrite ± arsenopyrite signals the beginning of the transition to the
287 late-ore stage in the Zimudang gold deposit (Fig. 2). With ore-stage collapse and
288 system cooling, sulfosalt minerals became stable, and zhengminghuaite, aktashite, and
289 christite precipitated and consumed remaining available Cu, Fe, Hg, and Tl in the
290 hydrothermal fluid. The greater abundance of zhengminghuaite relative to aktashite
291 and christite is probably related to higher Fe/Hg availability. With decrease in
292 temperature and increase in sulfidation state (f_{S2}), plus with a decreasing availability
293 of Cu, Fe, Hg, and Tl in the hydrothermal fluid, realgar became increasingly stable
294 and precipitated from the fluid. Zhengminghuaite and associated Hg- and Tl-sulfosalts
295 precipitated in response to the increasing f_{S2} by 1-2 log units and the decreasing
296 temperature by up to 100 °C during the transitional period from the main-ore to late-
297 ore stage. However, little is known about the solubility behavior of zhengminghuaite
298 and related sulfosalts, and their specific precipitation mechanisms and role in ore
299 formation are not yet very clear. Obviously, experiments and thermodynamic data are
300 required to clarify the stability relationships of zhengminghuaite with its associated
301 minerals and to more accurately constrain the physicochemical conditions under

302 which they formed.

303 ## ACKNOWLEDGMENTS AND FUNDING

304 We would like to thank and acknowledge Xia Yong and Fu Shaohong from
305 Institute of Geochemistry, Chinese Academy of Sciences, Yang Chengfu and Liu
306 Jianzhong from No. 105 Geological Team, Guizhou Bureau of Geology and Mineral
307 Exploration and Development, and all of the individuals from the Zimudang gold
308 mine for their help during the field work. The manuscript has been improved from the
309 valuable editorial efforts and constructive comments of Associate Editor Bin Chen,
310 the Technical Editor, and two anonymous reviewers. The research was jointly funded
311 by the National Natural Science Foundation of China (grants 42130804, 42002044,
312 40930423, and 40772060) and the Tianchi Talent Program of Xinjiang Uygur
313 Autonomous Region of China.

314 ## REFERENCES CITED

315 Altenberger, F., Raith, J.G., Bakker, R.J., and Zarasvandi, A. (2022) The Chah-Mesi
316 epithermal Cu-Pb-Zn-(Ag-Au) deposit and its link to the Meiduk porphyry
317 copper deposit, SE Iran: Evidence from sulfosalt chemistry and fluid inclusions.
318 Ore Geology Reviews, 142, 104732.

319 Balić-Žunić, T., Makovicky, E., Moëlo, Y. (1995) Contributions to the crystal
320 chemistry of thallium sulphosalts. III. The crystal structure of lorandite ($TlAsS_2$)
321 and its relation to weissbergite ($TlSbS_2$). Neues Jahrbuch für Mineralogie-
322 Abhandlungen, 168, 213–235.

Biagioni, C., Bonaccorsi, E., Moëlo, Y., and Orlandi P. (2014) Mercury-arsenic sulfosalts from the Apuan Alps (Tuscany, Italy). III. Aktashite, $Cu_6Hg_3As_4S_{12}$, and laffittite, $AgHgAsS_3$, from the Monte Arsiccio mine: Occurrence and crystal structure. Periodico di Mineralogia, 83, 1–18.

Botinelly, T., Neuerburg, G.J., and Conklin, N.M. (1973) Galkhaite, (Hg,Cu,Tl,Zn)(As,Sb)S_2, from the Getchell mine, Humboldt County, Nevada. Journal of Research of the U.S. Geological Survey, 1, 515–517.

Cline, J.S., Muntean, J.L., Gu, X.X., and Xia, Y. (2013) A comparison of Carlin-type gold deposits: Guizhou Province, Golden Triangle, Southwest China, and Northern Nevada, USA. Earth Science Frontiers, 20, 1–18.

Cooke, D.R., and Simmons, S.F. (2000) Characteristics and genesis of epithermal gold deposits. Reviews in Economic Geology, 13, 221–244.

Dickson, F.W., and Radtke, A.S. (1978) Weissbergite, $TlSbS_2$, a new mineral from the Carlin gold deposit, Nevada. American Mineralogist, 63, 720–724.

Dickson, F.W., Radtke, A.S., and Peterson, J.A. (1979) Ellisite, Tl_3AsS_3, a new mineral from the Carlin gold deposit, Nevada, and associated sulfide and sulfosalt minerals. American Mineralogist, 64, 701–707.

Dubé, B., Gosselin, P. Mercier-Langevin, P., Hannington, M., and Galley, A. (2007) Gold-rich volcanogenic massive sulphide deposits. In W.D. Goodfellow, Ed., Mineral Deposits of Canada: A Synthesis of Major Deposit-Types, District Metallogeny, the Evolution of Geological Provinces, and Exploration Methods. Geological Association of Canada, Mineral Deposits Division, Special

345 Publication, 5, 75–94.

346 Einaudi, M.T., Hedenquist, J.W., and Inan, E.E. (2003) Sulfidation state of fluids in
347 active and extinct hydrothermal systems: Transitions from porphyry to
348 epithermal environments. Society of Economic Geologists Special Publication,
349 10, 285–313.

350 Franklin, J.M., Gibson, H.L., Jonasson, I.R., and Galley, A.G. (2005) Volcanogenic
351 massive sulfide deposits. Economic Geology 100th Anniversary Volume, 523–
352 560.

353 Gabuda, S., Kozlova, S., Rizhikov, M., and Borisov, S. (2009) Closed-shell
354 interaction in the tetranuclear cluster As_4 in $Cu_6Hg_3As_4S_{12}$ crystal. Journal of
355 Molecular Structure: TEOCHEM, 907, 62–65.

356 Galley, A.G., Hannington, M.D., and Jonasson, I.R. (2007) Volcanogenic massive
357 sulphide deposits. In W.D. Goodfellow, Ed., Mineral Deposits of Canada: A
358 Synthesis of Major Deposit-Types, District Metallogeny, the Evolution of
359 Geological Provinces, and Exploration Methods. Geological Association of
360 Canada, Mineral Deposits Division, Special Publication, 5, 141–161.

361 Gu, X.X., Zhang, Y.M., Li, B.H., Dong, S.Y., Xue, C.J., and Fu, S.H. (2012)
362 Hydrocarbon-and ore-bearing basinal fluids: A possible link between gold
363 mineralization and hydrocarbon accumulation in the Youjiang basin, South China.
364 Mineralium Deposita, 47, 663–682.

365 Gu X.X., Zhang, Y.M., Wu, C.Y., Peng, Y.W., Li, B.H., Fu, S.H., Xia, Y., and Dong,
366 S.Y. (2013) The genetic relationship between Carlin-type gold deposits and

paleo-petroleum reservoirs in SW Guizhou, China: Evidence from organic petrology. Earth Science Frontiers, 20, 92–106 (in Chinese with English abstract).

Hannington, M.D., Poulsen, K.H., Thompson, J.F.H., and Sillitoe, R.H. (1997) Volcanogenic gold in the massive sulfide environment. Reviews in Economic Geology, 8, 325–356.

Hatert, F., and Burke, E.A.J. (2008) The IMA-CNMNC dominant-constituent rule revisited and extended. Canadian Mineralogist, 46, 717−728.

Hofstra, A.H., and Cline, J.S. (2000) Characteristics and models for carlin-type gold deposits. Reviews in Economic Geology, 13, 163–220.

Jian, W., Lehmann, B., Mao, J., Ye, H., Li, Z., Zhang, J., Zhang, H., Feng, J., and Ye, Y. (2014) Telluride and Bi-sulfosalt mineralogy of the Yangzhaiyu gold deposit, Xioqinling region, central China. The Canadian Mineralogist, 52, 883−898.

Kaplunnik, L.N., Pobedimskaya, E.A., and Belov, N.V. (1980) The crystal structure of aktashite, $Cu_6Hg_3As_4S_{12}$. Doklady Akademii Nauk SSSR, 251, 96−98 (in Russian).

Kasatkin, A.V., Plasil, J., Makovicky, E., Skoda, R., Agakhanov, A.A., and Tsyganko, M.V. (2022a) Pokhodyashinite, $CuTlSb_2(Sb_{1-x}Tl_x)AsS_{7-x}$, a new thallium sulfosalt from the Vorontsovskoe gold deposit, Northern Urals, Russia. Journal of Geosciences, 67, 41−51.

Kasatkin, A.V., Plášil, J., Makovicky, E., Chukanov, N.V., Škoda, R., Agakhanov, A.A., and Tsyganko, M.V. (2022b) Gungerite, $TlAs_5Sb_4S_{13}$, a new thallium sulfosalt with a complex structure containing covalent As-As bonds. American

389 Mineralogist, 107, 1164–1173.

390 Li, W., Cook, N.J., Ciobanu, C.L., Xie, G.Q., Wade, B.P., and Gilbert, S.E. (2019)
391 Trace element distributions in (Cu)-Pb-Sb sulfosalts from the Gutaishan Au-Sb
392 deposit, South China: Implications for formation of high fineness native gold.
393 American Mineralogist, 104, 425–437.

394 Liu, Y., Hu, K., Han, S.C., and Sun, Z.H. (2015) The nature of ore-forming fluids of
395 the Carlin-type gold deposit in Southwest China: A case from the Zimudang gold
396 deposit. Resource Geology, 65, 136–159.

397 Maroun, L.R.C., Cline, J.S., Simon, A., Anderson, P., and Muntean, J. (2017) High-
398 grade gold deposition and collapse breccia formation, Cortez Hills Carlin-type
399 gold deposit, Nevada, USA. Economic Geology, 112, 707–740.

400 Marumo, F. (1967) The crystal structure of nowackiite, $Cu_6Zn_3As_4S_{12}$. Zeitschrift für
401 Kristallographie, 124, 352–368.

402 Momma, K., and Izumi, F. (2011) VESTA 3 for three-dimensional visualization of
403 crystal, volumetric and morphology data. Journal of Applied Crystallography, 44,
404 1272–1276.

405 Moëlo, Y., Makovicky, E., Mozgova, N.N., Jambor, J.L., Cook, N., Pring., A., Paar,
406 W.H., Nickel, E.H., Graeser, S., Karup-Møller, S., Balić-Žunić, T., Mumme,
407 W.G., Vurro, F., Topa, D., Bindi, L., Bente, K. and Shimizu, M. (2008) Sulfosalt
408 systematics: A review report of the sulfosalt sub-committee of the IMA
409 Commission on Ore Mineralogy. European Journal of Mineralogy, 20, 7–46.

410 Nickel, E. H., and Grice, J. D. (1998). The IMA Commission on New Minerals and

411 Mineral Names: Procedures and guidelines on mineral nomenclature, 1998.
412 Mineralogy and Petrology, 64, 237–263.
413 Nowacki, W. (1982) Isotypy in aktashite $Cu_6Hg_3As_4S_{12}$ and nowackiite $Cu_6Zn_3As_4S_{12}$.
414 Soviet Physics-Crystallography, 27, 26–27.
415 Peng, Y.W., Gu, X.X., Zhang, Y.M., Liu, L., Wu, C.Y, and Chen, S.Y. (2014) Ore-
416 forming process of the Huijiabao gold district, southwestern Guizhou Province,
417 China: Evidence from fluid inclusions and stable isotopes. Journal of Asian Earth
418 Sciences, 93, 89–101.
419 Peters, S.G., Huang, J.Z., Li, Z.P., and Jing, C.G. (2007) Sedimentary rock-hosted Au
420 deposits of the Dian–Qian–Gui area, Guizhou, and Yunnan Provinces, and
421 Guangxi District, China. Ore Geology Reviews, 31, 170–204.
422 Radtke, A.S., Dickson, F.W., Slack, J.F., and Brown, K.L. (1977) Christite, a new
423 thallium mineral from the Carlin gold deposit, Nevada. American Mineralogist,
424 62, 421–425.
425 Radtke, A.S., Taylor, C.M., Erd, R.C., and Dickson, F.W. (1974) Occurrence of
426 lorandite $TlAsS_2$, at the Carlin gold deposit, Nevada. Economic Geology, 69,
427 121–123.
428 Shannon, R.D. (1976) Revised effective ionic radii and systematic studies of
429 interatomic distances in halides and chalcogenides. Acta Crystallographica, A32,
430 751–767.
431 Sheldrick, G.M. (2015a) SHELXT–Integrated space-group and crystal-structure
432 determination. Acta Crystallographica, A71, 3–8.

433 Sheldrick, G.M. (2015b) Crystal structure refinement with SHELXL. Acta
434 Crystallographica, C71, 3–8.
435 Sillitoe, R.H. (2000) Gold-rich porphyry deposits: Descriptive and genetic models and
436 their role in exploration and discovery. Reviews in Economic Geology, 13, 315–
437 345.
438 Simon, G., Kesler, S.E., and Chryssoulis, S. (1999) Geochemistry and textures of
439 gold-bearing arsenian pyrite, Twin Creeks, Nevada: Implications for deposition
440 of gold in Carlin-type deposits. Economic Geology, 94, 405–421.
441 Sinclair, W.D. (2007) Porphyry deposits. In W.D. Goodfellow, Ed., Mineral Deposits
442 of Canada: A Synthesis of Major Deposit-Types, District Metallogeny, the
443 Evolution of Geological Provinces, and Exploration Methods. Geological
444 Association of Canada, Mineral Deposits Division, Special Publication, 5,
445 223–243.
446 Slater, E.T., McDonald, A.M., and Kontak, D.J. (2019) Resolving primary and
447 retrograde sulfide and sulfosalt textures in the epithermal Ag-Zn-Pb-Sn-rich
448 Cortaderas Zone, Pirquitas Mine, Argentina. The Canadian Mineralogist, 57,
449 117–143.
450 Smith, D.G.W., and Nickel, E.H. (2007) A system for codification for unnamed
451 minerals: report of the Subcommittee for Unnamed Minerals of the IMA
452 Commission on New Minerals, Nomenclature and Classification. Canadian
453 Mineralogist, 45, 983–1055.
454 Spiridonov, E.P., Krapiva, L.Y., Gapeev, A.K., Stepanov, V.I., Prushinskaya, E.Y., and

Volgin, V.Y. (1981) Gruzdevite $Cu_6Hg_3Sb_4S_{12}$—a new mineral from the Chauvai antimony-mercury deposit, Central Asia. Doklady Akademii Nauk SSSR, 261, 971–976.

Su, W.C., Heinrich, C.A., Pettke, T., Zhang, X.C., Hu, R.Z., and Xia, B. (2009) Sediment-hosted gold deposits in Guizhou, China: Products of wall-rock sulfidation by deep crustal fluids. Economic Geology, 104, 73–93.

Taylor, B.E. (2007) Epithermal gold deposits. In W.D. Goodfellow, Ed., Mineral Deposits of Canada: A Synthesis of Major Deposit-Types, District Metallogeny, the Evolution of Geological Provinces, and Exploration Methods. Geological Association of Canada, Mineral Deposits Division, Special Publication, 5, 113–139.

Thompson, J.F.H., and Newberry, R.J. (2000) Gold deposits related to reduced granitic intrusions. Reviews in Economic Geology, 13, 377–400.

Vasil'ev, V.I., Pervukhina N.V., Borisov S.V., Magarill S.A., Naumov D.Yu., and Kurat'eva N.V. (2010) Aktashite $Cu_6Hg_3As_4S_{12}$ from the Aktash deposit, Altai, Russia: Refinement and crystal chemical analysis of the structure. Geology of Ore Deposits, 52, 656–661.

Vikentyev, I.V., Tyukova, E.E., Vikent'eva, O.V., Chugaev, A.V., Dubinina, E.O., Prokofiev, V.Y., and Murzin, V.V. (2019) Vorontsovka Carlin-style gold deposit in the North Urals: Mineralogy, fluid inclusion and isotope data for genetic model. Chemical Geology, 508, 144–166.

Zhang, Z.L., Yang, T.Y., Yang, S.H., Chen, L., Mao, Q, Ma, Y.G., He, W.T, and Ding,

K.S. (2017). Sulfosalt minerals of Ag and Pb-Bi-Cu, and its directing significance for minerogenic temperature in Dongjun Pb-Zn-Ag deposit of Erguna district, Inner Mongolia, China. Acta Petrologica Sinica, 33, 1827–1840.

FIGURE CAPTIONS

FIGURE 1. Photographs showing occurrence of the gold ore containing zhengminghuaite and associated hydrothermal minerals in the Zimudang gold deposit. (**a**) Fault- and fracture-controlled gold ore in bioclastic limestone consists mainly of realgar and calcite. (**b**) Hand specimen of zhengminghuaite-bearing gold ore composed of limestone and marl breccias cemented mainly by realgar and minor orpiment. (**c**) Late ore-stage mineral assemblage of drusy quartz, calcite, native arsenic, realgar, and orpiment, showing native arsenic replaced by realgar. (**d**) Main ore-stage quartz-pyrite veinlets crosscut and dislocated by a calcite-realgar veinlet. Photomicrographs **c** and **d** were taken under reflected plane-polarized light. Rlg = realgar; Orp = orpiment; As = native arsenic; Py = pyrite; Qz = quartz; Cal = calcite.

FIGURE 2. Paragenetic sequences of hydrothermal minerals in the Zimudang gold deposit.

FIGURE 3. Microscopic photographs and related back-scattered electron images showing zhengminghuaite and associated minerals. (**a**, **b**) Zhengminghuaite is fractured and occurs with aktashite, chalcopyrite, realgar, and pyrite. (**c**, **d**) Chalcopyrite was replaced by zhengminghuaite, while the latter was partially

replaced by realgar and coexists with tinny, fuzzy pyrite. Note also that zhengminghuaite partially has a straight boundary with realgar (upper right corner). (**e**, **f**) Earlier stage anhedral to subhedral pyrite is enclosed by zhengminghuaite, which coexists with aktashite and replaced chalcopyrite. All these minerals are overgrown and partially replaced by realgar. Photomicrographs **a**, **c**, and **e** were taken under reflected plane-polarized light, and **b**, **d**, and **f** are back-scattered electron images. Zmh = zhengminghuaite; Ats = aktashite; Ccp = chalcopyrite; other symbols as in Figure 1.

FIGURE 4. Crystal structure of zhengminghuaite as seen down [0001]. Polyhedra: ochre = Fe site; dark cyan = Cu1 site; blue = Cu2 site. Circles: green = As1 site; violet = As2 site; yellow = S sites.

FIGURE 5. $[As_4S_{12}]^{12-}$ group in the structure of zhengminghuaite. Symbols as in Figure 4.

FIGURE 6. Log f_{S2} vs. T diagram showing stability fields of Fe minerals (bold lines), As minerals, Sb minerals, and As-S liquid (dashed lines). Deposition fields of drusy quartz + pyrite ± arsenopyrite and realgar in the late ore-stage at Zimudang are highlighted by dark and medium shading, respectively. The shaded arrow shows the change trajectory of mineral assemblages due to the decreasing temperature and increasing sulfidation state of the ore fluid. Modified after Simon et al. (1999) and Einaudi et al. (2003).

TABLES

TABLE 1. Chemical composition (wt.%) and unit formula (apfu) for zhengminghuaite based on electron microprobe data.

TABLE 2. X-ray powder diffraction data (*d* in Å) for zhengminghuaite.

TABLE 3. Selected bond lengths (in Å) for zhengminghuaite.

TABLE 4. Site occupancies, refined and calculated site scattering for Fe and Cu sites in zhengminghuaite.

TABLE 5. Predominant-constituents in the structural sites of zhengminghuaite and the known nowackiite isotypic series members.

SUPPLEMENTAL MATERIALS

APPENDIX TABLE 1. Crystal data and summary of parameters describing data collection and refinement for zhengminghuaite.

APPENDIX TABLE 2. Atomic coordinates, site occupancies, and equivalent isotropic and anisotropic atomic displacement parameters ($Å^2$) for zhengminghuaite.

ONLINE MATERIAL: The Crystallographic Information File (CIF) for zhengminghuaite.

TABLE 1. Chemical composition (wt.%) and unit formula (apfu) for zhengminghuaite based on electron microprobe data

Constituent	Mean (n = 8)	Range	S.D. (σ)	apfu	Probe standard
Cu	26.73	26.50–26.96	0.13	5.92	chalcopyrite
Fe	6.31	5.66–6.79	0.41	1.59	marcasite
Hg	16.31	15.51–17.56	0.63	1.15	cinnabar
Zn	1.73	1.48–2.34	0.28	0.37	sphalerite
As	20.98	20.43–21.21	0.24	3.94	synthetic GaAs
Sb	0.18	0.05–0.28	0.08	0.02	synthetic Sb_2Te_3
S	27.16	26.75–27.56	0.31	11.93	cinnabar
Total	99.40	98.71–99.87	0.46		

Notes : n = number of analyses, S.D. = standard deviation.

TABLE 2. X-ray powder diffraction data (d in Å) for zhengminghuaite

I_{cacl} (%)	d	h	k	l	I_{cacl} (%)	d	h	k	l
5	7.2548	1	0	1	20	1.9676	1	4	-3
21	6.7687	1	1	0	7	1.9539	0	6	0
23	4.9491	0	2	1	7	1.8867	-3	-4	1
11	4.2964	0	1	2	**97**	**1.8825**	**1**	**3**	**4**
10	3.9951	-2	-1	-1	**82**	**1.8773**	**5**	**2**	**0**
8	3.6274	2	0	2	5	1.6922	-4	-4	0
65	**3.0785**	**0**	**0**	**3**	6	1.6497	6	0	3
100	**3.0670**	**-1**	**-3**	**-1**	6	1.6451	0	5	4
10	2.8023	1	1	3	**89**	**1.6060**	**1**	**3**	**-5**
89	**2.6586**	**-1**	**-3**	**2**	**81**	**1.6028**	**5**	**2**	**3**
21	2.5583	4	1	0	**83**	**1.6012**	**2**	**6**	**-1**
6	2.4183	3	0	3	7	1.5392	0	0	6
5	2.3241	2	3	2	20	1.5335	2	6	2
8	2.2773	2	2	-3	55	1.3293	-2	-6	4
13	2.2726	5	0	-1	20	1.2225	1	3	7
8	2.2653	0	1	-4	21	1.2204	2	6	5
10	2.2562	3	3	0	10	1.2225	1	3	7
5	2.1544	2	4	1	19	1.2182	6	5	1
14	2.1482	0	2	4	5	1.1903	-5	-2	6
8	2.0907	5	0	2	20	1.0879	1	3	-8
9	2.0529	1	5	-1	18	1.0849	6	5	4
7	2.0476	2	1	4	18	1.0839	3	9	0
6	1.9975	2	4	-2					

Notes: Intensity as well as d, h, k, and l were calculated using the software VESTA (Momma and Izumi, 2011) on the basis of the structural model given in Table 3. Only reflections with I_{calc} > 5 % are listed. The intensities of the eight strongest lines are given in bold characters.

TABLE 3. Selected bond lengths (in Å) for zhengminghuaite

Fe1-S1	2.378(8)	Cu1-S2	2.272(8)
Fe1-S1	2.383(11)	Cu1-S2	2.319(9)
Fe1-S3	2.395(10)	Cu1-S3	2.319(9)
Fe1-S4	2.432(11)	Cu1-S1	2.349(8)
average	2.397	average	2.315
Cu2-S4	2.316(11)	As1-S2	2.253(7)
Cu2-S3	2.317(9)	As1-S1	2.259(9)
Cu2-S2	2.326(10)	As1-S4	2.298(9)
Cu2-S4	2.332(9)	average	2.270
average	2.323		
		As2-S3	$2.278(9)^{\times 3}$

TABLE 4. Site occupancies, refined and calculated site scattering for Fe and Cu sites in zhengminghuaite

Site	Site occupancy	Calculated site scattering	Refined site scattering
Fe	$Fe_{0.53}Hg_{0.35}Zn_{0.12}$	45.4	44.4
Cu1	$Cu_{1.00}$	29.0	29.0
Cu2	$Cu_{0.98}Hg_{0.02}$	30.0	29.0

TABLE 5. Predominant-constituents in the structural sites of zhengminghuaite and the known nowackiite isotypic series members

Mineral name	Site occupation				Reference
	Me^{1+}	Me^{2+}	*Pn*	*Ch*	
zhengminghuaite	Cu	Fe	As	S	This work
nowackiite	Cu	Zn	As	S	Marumo (1967); Nowacki (1982)
aktashite	Cu	Hg	As	S	Kaplunnik et al. (1980); Vasil'ev et al. (2010); Biagioni et al. (2014)
gruzdevite	Cu	Hg	Sb	S	Spiridonov et al. (1981)

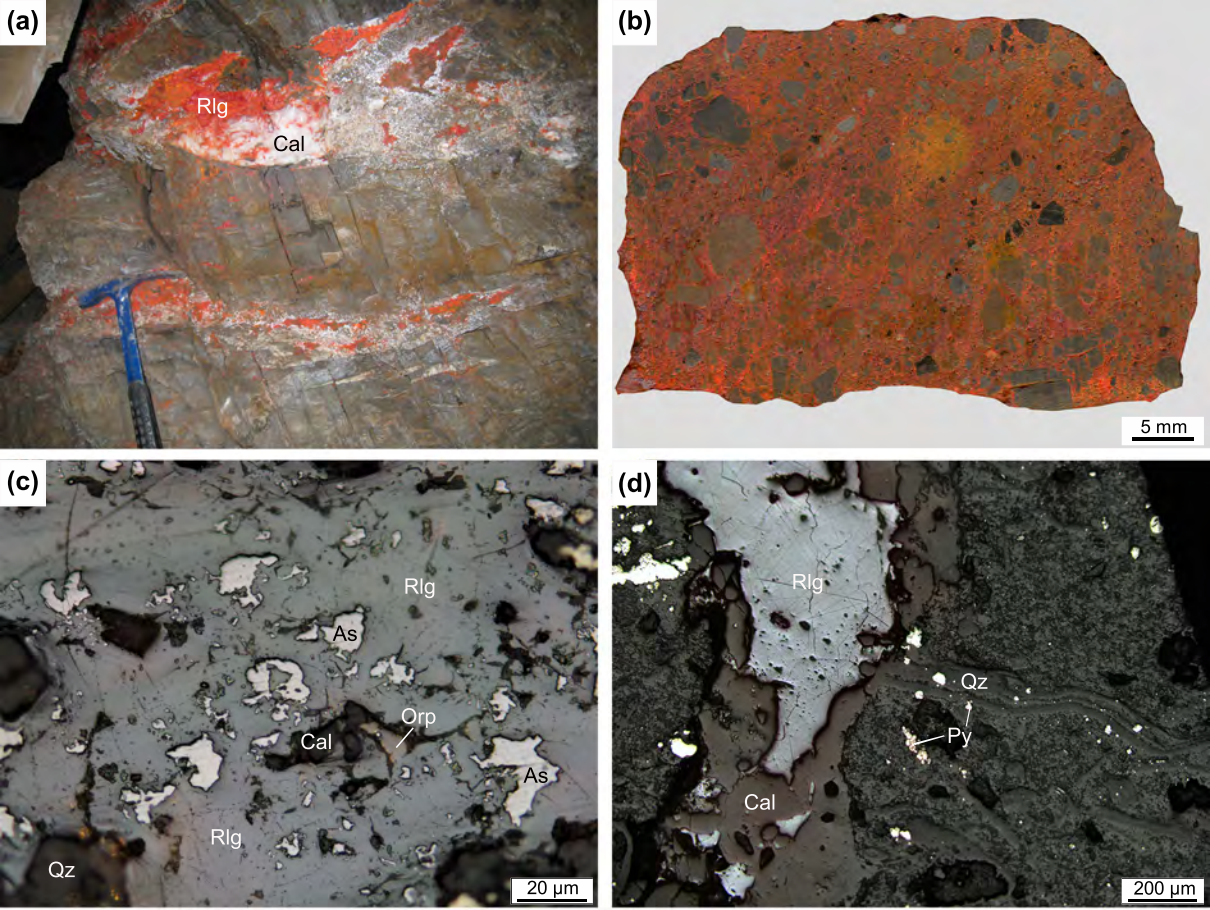

Figure 1, Gu et al., *AM*

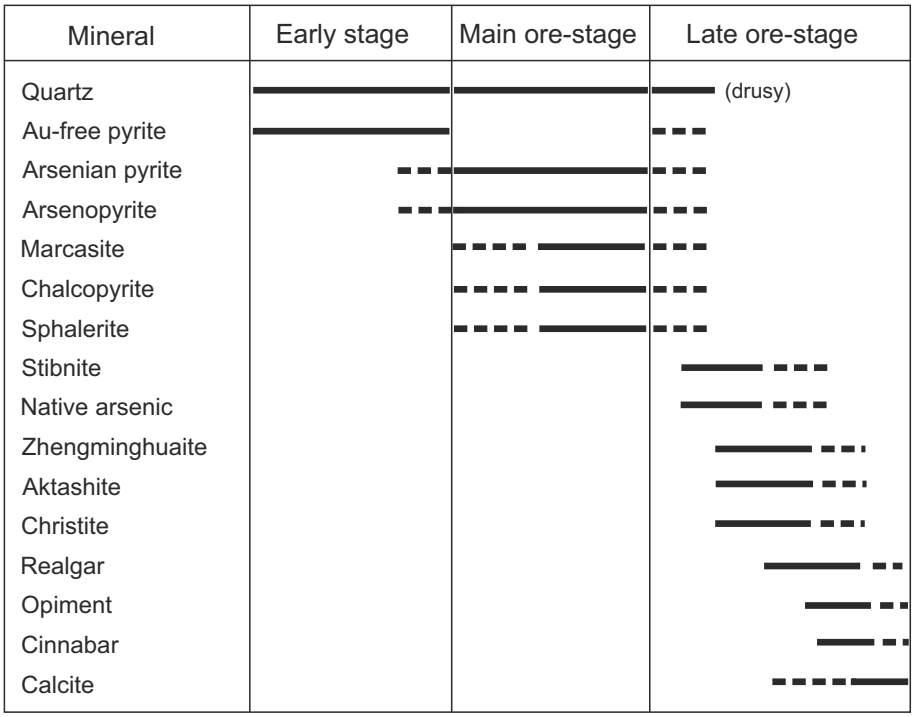

Figure 2, Gu et al., *AM*

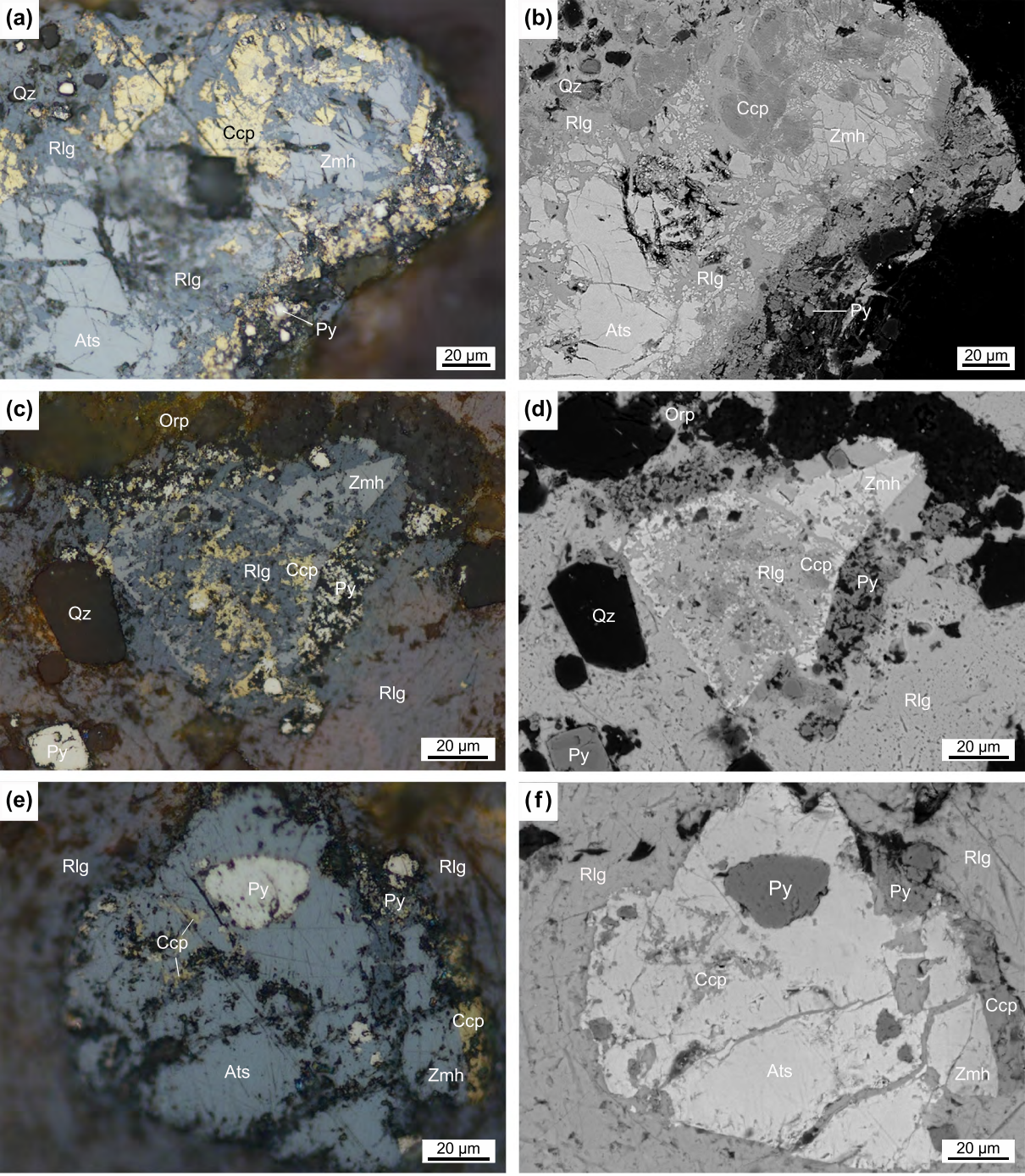

Figure 3, Gu et al., *AM*

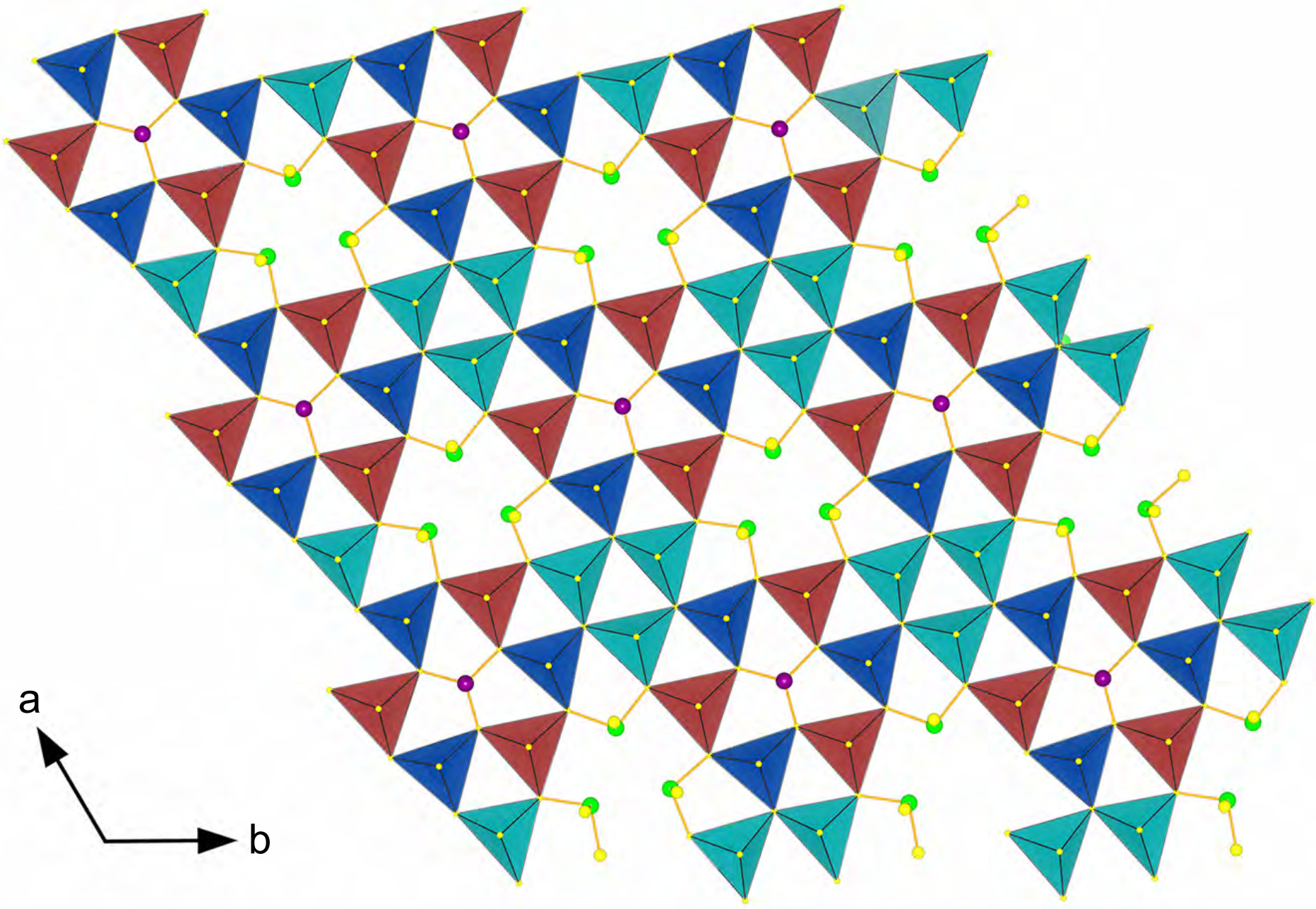

Figure 4, Gu et al., *AM*

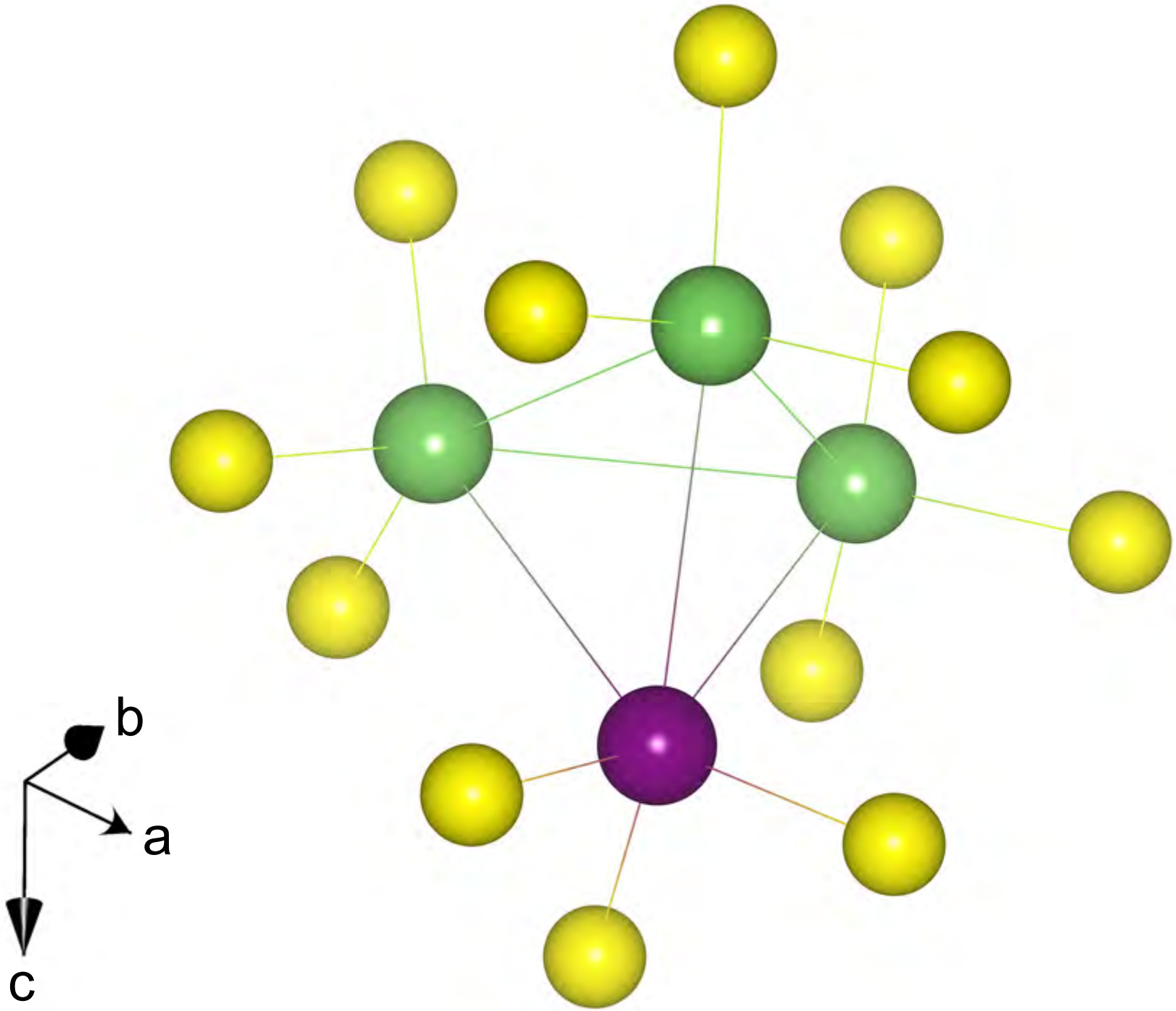

Figure 5, Gu et al., *AM*

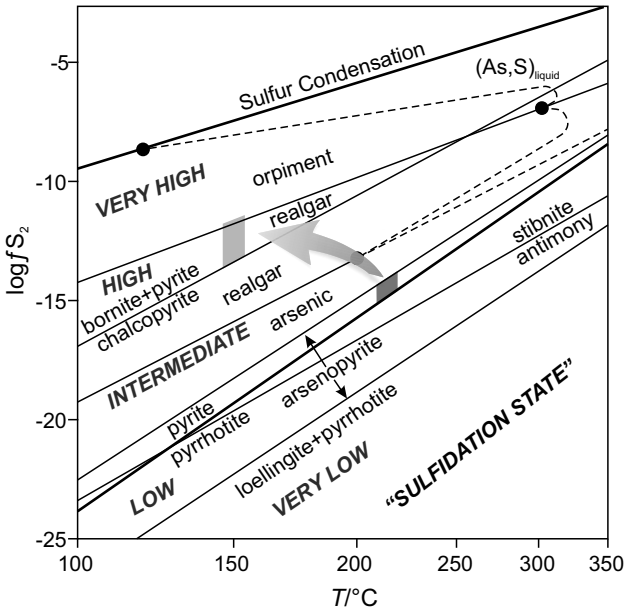

Figure 6, Gu et al., *AM*